Interaction of a Cumulus Cloud Ensemble with the Large-Scale Environment. Part III: Semi-Prognostic Test of the Arakawa-Schubert Cumulus Parameterization

STEPHEN J. LORD[1]

Department of Atmospheric Sciences, University of California, Los Angeles 90024

(Manuscript received 26 August 1980, in final form 14 September 1981)

ABSTRACT

The verification of the Arakawa and Schubert (1974) cumulus parameterization is continued using a semi-prognostic approach. Observed data from Phase III of GATE are used to provide estimates of the large-scale forcing of a cumulus ensemble at each observation time. Instantaneous values of the precipitation and the warming and drying due to cumulus convection are calculated using the parameterization.

The results show that the calculated precipitation agrees very well with estimates from the observed large-scale moisture budget and from radar observations. The calculated vertical profiles of cumulus warming and drying also are quite similar to the observed. It is shown that the closure assumption adopted in the parameterization (the cloud-work function quasi-equilibrium) results in errors of generally <10% in the calculated precipitation. The sensitivity of the parameterization to some assumptions of the cloud ensemble model and the solution method for the cloud-base mass flux is investigated.

1. Introduction

In Part I of this series of papers Arakawa and Schubert (1974) developed a cumulus cloud parameterization for use in large-scale numerical prediction models. This cumulus parameterization is closed by the assumption of a balance between the generation of moist convective instability on the large-scale and its destruction by the clouds themselves. Some observational evidence for this assumption, the cloud-work function quasi-equilibrium, has been presented in Part II of this series (Lord and Arakawa, 1980). The purpose of this paper is to continue the observational verification of the Arakawa-Schubert cumulus parameterization.

To place the methodology used here in the proper perspective it may be appropriate to summarize three possible ways of using observed large-scale data, such as those gathered during the recent GARP Atlantic Tropical Experiment (GATE), in the verification of a cumulus parameterization. The first approach is a purely prognostic one in which the cumulus parameterization is used in a large-scale numerical prediction model. Large-scale data are used to define an initial condition for the model, and cumulus parameterization is used to determine the precipitation and large-scale warming and drying due to cumulus clouds at each model time step. After a given number of time steps the model results are compared with observations and the performance of the cumulus parameterization scheme is thereby assessed. Although direct testing of a cumulus parameterization in a numerical prediction model is desirable, an unambiguous assessment of the parameterization may be difficult with this approach due to other modeling errors such as initialization of the large-scale model, space and time truncation errors, effect of an artificial upper boundary, or the parameterization of physical processes other than cumulus convection.

The second approach is purely diagnostic. Observed estimates of the horizontal and vertical advections of thermodynamical quantities may be combined with observed temperature and moisture tendencies to produce residuals in the large-scale budgets (Fig. 1) denoted by the apparent heat source (Q_1) and moisture sink (Q_2) which are defined as (Yanai *et al.*, 1973)

$$Q_1 \equiv \frac{\partial \bar{s}}{\partial t} + \bar{\mathbf{V}} \cdot \nabla \bar{s} + \bar{\omega} \frac{\partial \bar{s}}{\partial p} \tag{1}$$

and

$$Q_2 \equiv -L\left[\frac{\partial \bar{q}_v}{\partial t} + \bar{\mathbf{V}} \cdot \nabla \bar{q}_v + \bar{\omega} \frac{\partial \bar{q}_v}{\partial p}\right]. \tag{2}$$

Here $s = c_pT + gz$ is the dry static energy, c_p the specific heat of air at constant pressure, T the temperature, g the acceleration of gravity, z the height above sea level, $\mathbf{V}$ the horizontal velocity, ∇ the horizontal gradient operator, ω the vertical p-velocity, p the pressure, L the latent heat per unit mass of water vapor, and q_v the water vapor mixing ratio. The overbar denotes a large-scale horizontal average.

[1] Current affiliation: Atlantic Oceanographic and Meteorological Laboratories, National Hurricane Research Laboratory, NOAA, Coral Gables, FL 33146.

0022-4928/82/010088-16$08.00

From Q_1 and Q_2, and estimates of both the surface thermodynamical fluxes and the large-scale heating rate due to radiation (Q_R), the precipitation from a vertical column and the vertical distributions of warming and drying by cumulus clouds may be diagnosed assuming that the vertical eddy transports are primarily due to the clouds (e.g., Nitta, 1972; Thompson *et al.*, 1979). In addition, if a hypothetical cloud ensemble model is used, the spectrum of cumulus mass flux may be diagnosed (e.g., Ogura and Cho, 1973; Yanai *et al.*, 1973; Nitta, 1975, 1977; Johnson, 1976, 1980). However, since the observed temperature and moisture tendencies are already used in estimating Q_1 and Q_2 [see Eqs. (1) and (2)], the diagnostic approach cannot verify the prognostic capability of a cumulus parameterization.

The third approach, used in this paper, is called the "semi-prognostic" approach. The observed estimates of advection, surface fluxes and radiative heating are used to estimate the large-scale forcing of a cumulus ensemble (see Part I) at a given observation time. These observations and the cumulus parameterization, which consists of a cloud ensemble model and a closure assumption (Fig. 1), are combined to predict the cumulus mass flux spectrum at each observation time. The associated precipitation and cumulus warming and drying are then calculated from the predicted mass flux spectrum. It is important to note that Q_1 and Q_2 are the *results* of the semi-prognostic calculations, unlike in the diagnostic approach described above. Also note that the semi-prognostic study does not march in time (as in the prognostic approach) and therefore it is free from any modeling errors other than those in the cumulus parameterization.

The cumulus parameterization may be directly evaluated by comparison of the calculated and observed Q_1 and Q_2 since the two are not constrained to agree. In the semi-prognostic approach exact agreement between the calculated results and observed values cannot be expected even if they are both error-free. The calculated results represent instantaneous values and do not necessarily correspond to the observed values which are usually averaged over a finite time interval. However, the locus of semi-prognostic values should form an envelope which closely follows the observed values as shown schematically in Fig. 2.

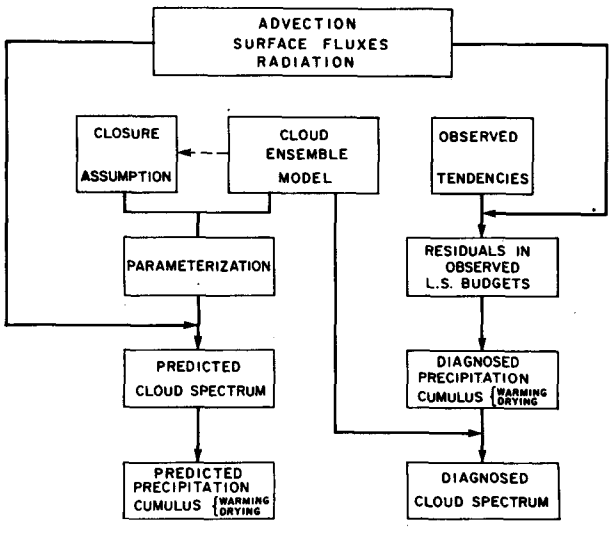

FIG. 1. A schematic diagram showing the role of large-scale observed data in the verification of a cumulus parameterization.

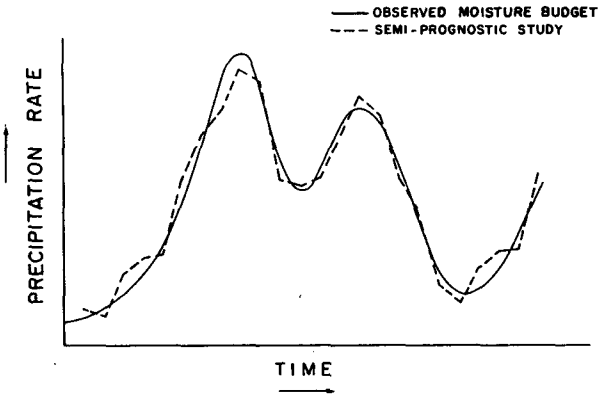

FIG. 2. A schematic diagram comparing the precipitation rates obtained from a semi-prognostic approach and from the observed moisture budget.

The semi-prognostic approach has been used by Ramanathan (1980) who has shown predicted precipitation rates for a monsoon depression forming over the Bay of Bengal. Krishnamurti *et al.* (1980) have discussed the prediction of precipitation rates during Phase III of GATE using several different cumulus parameterization schemes.

The data and procedures used in this semi-prognostic study are described in Section 2. The results are presented in Section 3 and a summary and discussion are given in Section 4. Frequent references are made to a companion paper in this issue (Lord *et al.*, 1982, hereafter referred to as Part IV) which describes the Arakawa-Schubert parameterization as applied to a prognostic model of the large-scale atmospheric circulations.

2. Data and procedure

The large-scale data are taken from the *B*- and *A*/*B*-scale network data for Phase III of GATE as analyzed by Thompson *et al.* (1979). Values of $\bar{T}$, $\bar{q}_v$, their horizontal and vertical derivatives, and all velocity components are given for the center of the *B*-scale array every 3 h at the surface and at 25 mb intervals from 1000 to 100 mb. Details of the analysis procedure are given in Thompson *et al.*

A discretized cumulus cloud ensemble model, de-

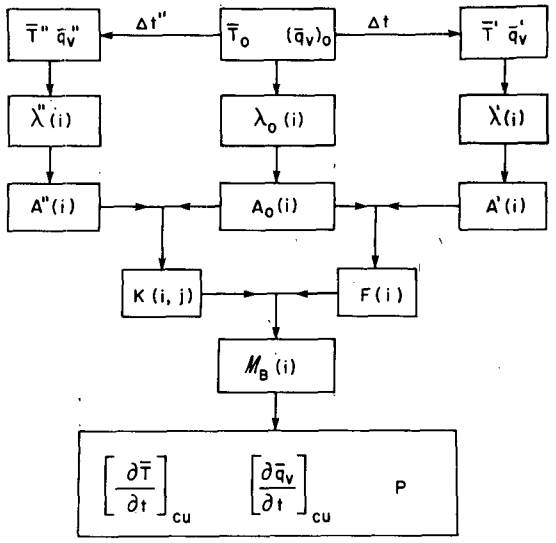

FIG. 3. A schematic diagram showing the procedure for this semi-prognostic study. See text for details.

scribed in Part IV, is used to determine the properties of subensembles which have their tops at fixed pressure levels $\hat{p}$. The cloud-top levels chosen for this study are $\hat{p}(i)$, $i = 1, 2, \cdots 16, 17, 18$, which are located at 100, 150, $\cdots$ 850, 900, 937.5 mb, respectively. Variables at these levels are assumed representative of the layers whose boundaries are at 75, 125, $\cdots$ 875, 925, 950 mb. The subcloud layer (SCL) top is chosen to be at 950 mb.

Cloud subensemble variables are identified by the cloud-top level index i. For example, $\lambda(i)$ and $A(i)$ are the fractional entrainment rate and the cloud-work function, respectively, of the ith subensemble. Recall that from Parts I and II that the cloud-work function is a generalized measure of the moist convective instability in the large-scale environment and is given in continuous form by

$$A(i) = \int_{z_B}^{\hat{z}(i)} \frac{g}{\bar{T}(z)} \eta(z, i)[T_{vc}(z, i) - \bar{T}_v(z)]dz, \quad (3)$$

where $\hat{z}(i)$ is the cloud-top height, z_B is the height of the SCL top, $\eta(z, i)$ is the subensemble mass flux normalized at cloud base, and $T_{vc}(z, i)$ and $\bar{T}_v(z)$ are the subensemble and environmental virtual temperatures, respectively.

The subensemble variables $\eta(z, i)$ and $T_{vc}(z, i)$, and thus $A(i)$, are determined by the vertical distributions of $\bar{T}$ and $\bar{q}_v$, the cloud-base water vapor mixing ratio and moist static energy q_{vm} and h_m, and z_B. The cloud-base variables are calculated from data at the 975 and 1000 mb levels as

$$q_{vm} = \tfrac{1}{2}[\bar{q}_v(975) + \bar{q}_v(1000)]$$

and

$$h_m = c_p T_B + g z_B + L q_{vm},$$

where the pressure level of the observed variable is enclosed in parentheses, and T_B is a temperature extrapolated to the top of the SCL and is determined from the potential temperature θ,

$$T_B = \tfrac{1}{2}[\theta(975) + \theta(1000)] \times \left[\frac{950}{1000}\right]^{R/c_p}.$$

A simple ice-phase parameterization (Lord, 1978) is included to account for the increased cloud buoyancy due to the release of latent heat of fusion.

The procedure for obtaining the predicted cloud-base mass flux spectrum $\mathcal{M}_B(i)$ at each observation time is as follows. The $\mathcal{M}_B(i)$ are determined by solving a discretized form of the integral equation (158) of Part I which is written as

$$\mathcal{M}_B(i)\Delta t > 0 \quad \text{and}$$

$$\sum_{j=1}^{i_{\max}} [K(i, j)\mathcal{M}_B(j)\Delta t] + F(i)\Delta t = 0 \quad (4a)$$

or

$$\mathcal{M}_B(i)\Delta t = 0 \quad \text{and}$$

$$\sum_{j=1}^{i_{\max}} [K(i, j)\mathcal{M}_B(j)\Delta t] + F(i)\Delta t < 0 \quad (4b)$$

for $1 \leqslant i \leqslant i_{\max}$. Here $i_{\max}$ is the number of existing subensembles, $K(i, j)$ is a discrete form of the mass flux kernel which gives the stabilization of the ith subensemble through modification of the large-scale environment by the jth subensemble, and $F(i)$ is the large-scale forcing for the ith subensemble. Procedures for the determination of $F(i)$ and $K(i, j)$ involve the calculation of cloud-work function changes due to large-scale processes and cloud processes, respectively. These procedures are summarized below.

Let the temperature and water vapor mixing-ratio data at a given observation time be denoted by $\bar{T}_0$ and $(\bar{q}_v)_0$ as shown in Fig. 3. From these data the fractional entrainment rate $\lambda_0(i)$ and the cloud-work function $A_0(i)$ are calculated for clouds that are nonbuoyant at each $\hat{p}(i)$. Let the observed large-scale advective temperature and moisture changes be denoted by $(\partial\bar{T}/\partial t)_{\text{ADV}}$ and $(\partial\bar{q}_v/\partial t)_{\text{ADV}}$, respectively, and let the radiative temperature changes be given by $(\partial\bar{T}/\partial t)_{\text{RAD}} \equiv Q_R/c_p$, where Q_R is taken from the daily 24 h mean values over the GATE A/B array of Cox and Griffith (1978). The large-scale temperature and moisture fields are modified by the advective and radiative processes over a time Δt to give

$$\bar{T}' = \bar{T}_0 + \left[\left(\frac{\partial \bar{T}}{\partial t}\right)_{\text{ADV}} + \left(\frac{\partial \bar{T}}{\partial t}\right)_{\text{RAD}}\right]\Delta t \quad (5a)$$

and

$$\bar{q}_v' = (\bar{q}_v)_0 + \left(\frac{\partial \bar{q}_v}{\partial t}\right)_{\text{ADV}} \Delta t. \quad (5b)$$

Next, the modified fractional entrainment rate $\lambda'(i)$

and cloud-work function $A'(i)$ are calculated from the large-scale fields $\bar{T}'$ and $\bar{q}'_v$. The large-scale forcing for each cloud type is then calculated from

$$F(i) = \frac{A'(i) - A_0(i)}{\Delta t}. \quad (6)$$

The time interval $\Delta t = 30$ min is used in this study.

The calculation of the discretized mass flux kernel $K(i, j)$ proceeds as follows. First, the $\bar{T}_0$ and $(\bar{q}_v)_0$ are modified by an arbitrarily chosen small amount of cloud-base mass flux of the jth subensemble integrated over a time interval $\Delta t''$, $\mathcal{M}''_B(j)\Delta t''$, to give

$$\bar{T}'' = \bar{T}_0 + \delta_j[\bar{T}]\mathcal{M}''_B(j)\Delta t'', \quad (7a)$$

$$\bar{q}''_v = (\bar{q}_v)_0 + \delta_j[\bar{q}_v]\mathcal{M}''_B(j)\Delta t'', \quad (7b)$$

where the double prime indicates a value used in the kernel calculation and $\delta_j[\bar{T}]$ and $\delta_j[\bar{q}_v]$ represent the time changes in temperature and water vapor mixing ratio per unit cloud-base mass flux of the jth subensemble. The δ_j are given by discrete forms of the cumulus terms in the large-scale thermodynamical budget equations (74) and (75) of Part I as developed in Part IV.

Second, the cloud-base variables h_m and q_{vm} are modified due to cumulus processes following the assumption adopted in this semi-prognostic study that the SCL top remains constant at 950 mb. Taking into account the large-scale compensating subsidence due to the mass flux into the jth subensemble, $\mathcal{M}''_B(j)\Delta t''$, this assumption suggests a modification of h_m and q_{vm} according to

$$h''_m = h_m(1 - a'') + a''\bar{h}(950), \quad (8a)$$

$$q''_{vm} = q_{vm}(1 - a'') + a''\bar{q}_v(950), \quad (8b)$$

where $a'' = \mathcal{M}''_B(j)\Delta t''/(\rho_B z_B)$, ρ_B is the mean density of SCL air and the second term in (8) represents the fraction of subsiding air from above the SCL. The effect of (8) is to warm and dry the SCL air due to cumulus convection.

Finally, the $K(i, j)$ are calculated from

$$K(i, j) = \frac{A''(i) - A_0(i)}{\mathcal{M}''_B(j)\Delta t''}, \quad (9)$$

where $A''(i)$ is the cloud-work function calculated from $\bar{T}''$, $\bar{q}''_v$, h''_m and q''_{vm}. Thus $K(i, j)$ represents the time rate of change in the cloud-work function of the ith subensemble due to modification of the large-scale environment by a unit mass flux of the jth subensemble.

The calculated $F(i)$ and $K(i, j)$ are substituted into (4) which is then solved for the $\mathcal{M}_B(i)$ using the simplex linear programming algorithm (Gass, 1975). The rates of precipitation P and cumulus warming $[\partial\bar{T}/\partial t]_{CU}$ and drying $\partial\bar{q}_v/\partial t]_{CU}$ for each layer are calculated and the results are compared to the estimates from observations.

The simplex algorithm gives an optimal solution of (4) subject to the constraints of non-negative $\mathcal{M}_B(i)$ and a minimized linear objective function

$$Z = \sum_{i=1}^{i_{max}} c(i)\left\{\sum_{j=1}^{i_{max}} [K(i, j)\mathcal{M}_B(j)\Delta t] + F(i)\right\}, \quad (10)$$

where the $c(i)$ are specified weighting factors (Hack and Schubert, 1976). In this study $c(i) = 1.0$ is assumed for all i. Comparison of (10) and (4a) shows that the simplex algorithm minimizes the difference between the large-scale forcing and the cumulus stabilization. Further details concerning this application of the simplex algorithm may be found in Part IV. The sensitivity of the solutions of (4) to the solution method is examined in Section 3e.

In this study any possible changes in h_m and q_{vm} due to large-scale surface fluxes, entrainment at the SCL top, horizontal advection and radiation are neglected because the vertical resolution of the data is not sufficient to provide good estimates of these subcloud layer processes. Thus, $F(i)$ calculated by (5)–(6) corresponds to the cloud-layer forcing given by (B33) of Part I. Schubert (1973) using the mixed-layer model for the SCL discussed in Part I, has shown that the mixed-layer forcing is a small fraction of the cloud-layer forcing under most circumstances. It is important to note that neglect of the mixed-layer forcing does not imply that all boundary-layer processes are ignored. For example, frictional convergence within the boundary layer is manifested in the observed vertical velocity near the SCL top and is thus included as part of the cloud-layer forcing.

3. Results

a. Case Q

Case Q is the quasi-equilibrium experiment. This case follows the procedure outlined in Section 2. The remaining cases have the same procedure unless otherwise noted.

Fig. 4 is a time series of the large-scale cloud-layer forcing for each cloud type. The ordinate is the cloud-top pressure $\hat{p}$ for each subensemble. Only positive cloud-layer forcings are shown. The forcing is a maximum for clouds with tops at 300 mb. The maxima on 2, 9, 13 and 16–17 September correspond to the passage of the easterly wave troughs T_2, T_4, T_5 and T_6 described by Thompson *et al.* (1979). The maximum on 4–5 September corresponds to a disturbed period described by Houze (1977). Fig. 5 shows the time average of the forcing displayed in Fig. 4.

Fig. 6 is a time series of precipitation rates (mm day^{-1}) from 1–18 September estimated by the Arakawa-Schubert parameterization, the observed moisture budget, and the observed radar measure-

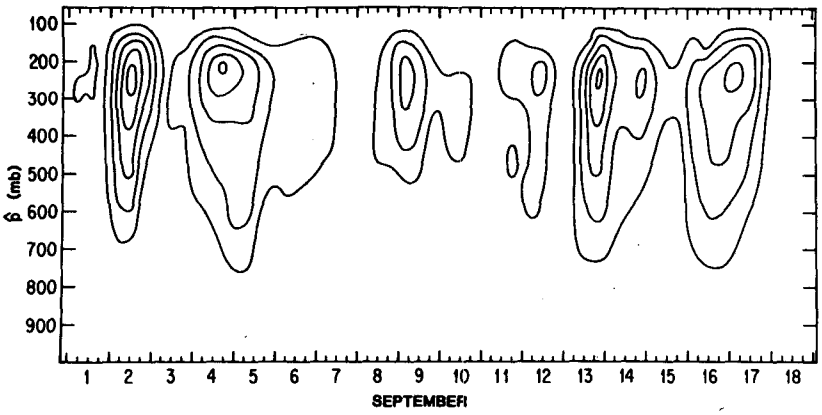

FIG. 4. A time series of the cloud-layer forcing (kJ kg^{-1} day^{-1}) for each cloud type for case Q. The contour interval is 1 kJ kg^{-1} day^{-1}. The ordinate is the cloud-top pressure $\hat{p}$ (mb).

ments. The precipitation rates P_{AS} calculated from the Arakawa-Schubert parameterization are calculated from

$$P_{AS} = \sum_{i=1}^{i_{max}} \sum_{k=i}^{KF} c_0 \Delta z(k) q_l(k, i) \eta(k - \tfrac{1}{2}, i) \mathcal{M}_B(i), \quad (11)$$

where the summations over i and k are for all subensembles and for all layers penetrated by each subensemble, respectively, KF is the index of the layer immediately above the SCL, $c_0 = 2.0 \times 10^{-3}$ m^{-1} is an empirically chosen constant precipitation parameter, $\Delta z(k)$ is the thickness of layer k, $q_l(k, i)$ is the layer-averaged cloud suspended liquid water mixing ratio and $\eta(k - \frac{1}{2}, i)$ is the normalized subensemble mass flux at the top of layer k. The estimate from the observed moisture budget P_{Q2} is calculated from

$$P_{Q2} = \int_{100}^{p_s} \frac{Q_2}{L} \frac{dp}{g} + E_S,$$

where E_S is an estimated surface evaporation rate calculated using the method of Deardorff (1972) and p_s is the surface pressure. The precipitation rates derived from radar estimates P_{RA} are shown every 6 h and are weighted mean values of the hourly data calculated by Hudlow and Patterson (1979). The averaging, described by Lord (1978), brings the val-

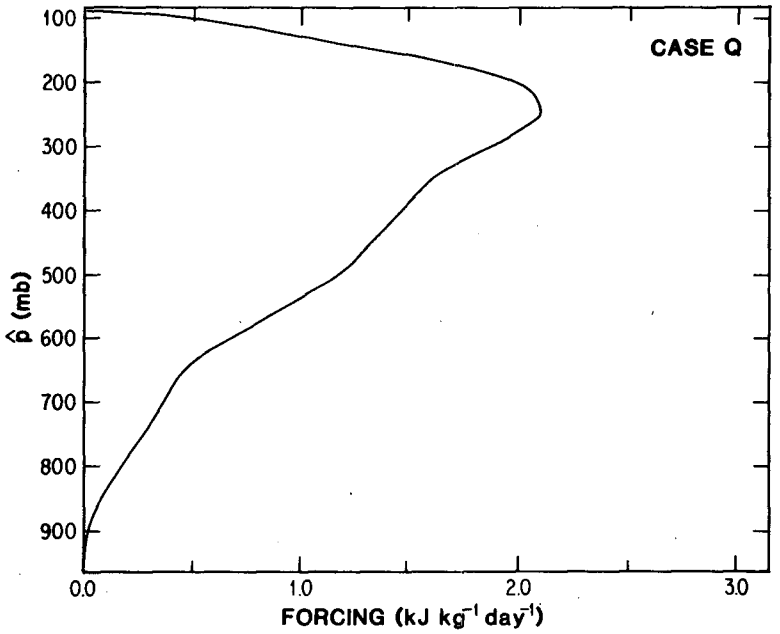

FIG. 5. The time-averaged cloud-layer forcing for case Q over the period 1–18 September. The ordinate is the cloud-top pressure $\hat{p}$ (mb).

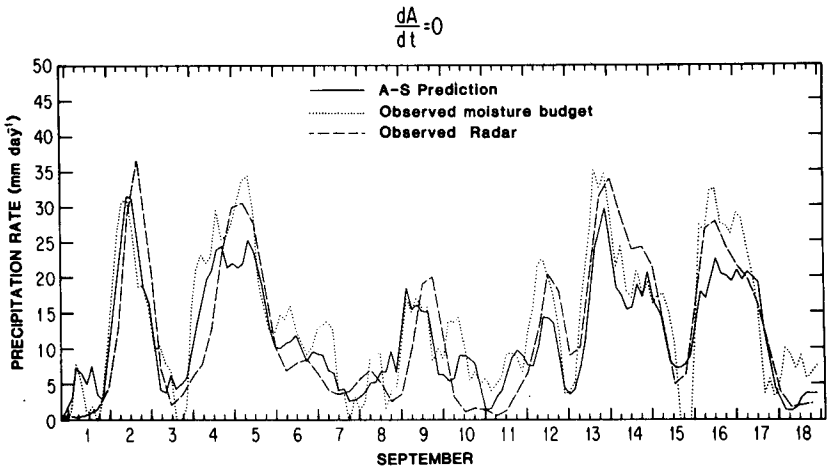

FIG. 6. A time series of precipitation rates (mm day^{-1}) from 1–18 September estimated by case Q, the observed moisture budget and radar.

ues of P_{RA} into closer agreement with the values of P_{Q2} but does not, of course, modify the mean value over the 18-day period. The average precipitation rates are $\tilde{P}_{Q2}$ = 14.3 mm day^{-1} and $\tilde{P}_{RA}$ = 12.4 mm day^{-1} where the tilde represents a time average over 1–18 September.

The values of P_{AS} agree closely in both magnitude and phase with the two independent estimates from observations, P_{Q2} and P_{RA}. The peak values of P_{AS} on 2 and 9 September are almost identical to those of the P_{Q2} estimate. The observed variations of precipitation rates during disturbed periods on 4–5, 12, 13 and 16 September are well captured by the parameterized values but the peak values are 30–40% smaller than the P_{Q2} estimate. The values of P_{AS} during undisturbed periods show generally good agreement with P_{RA} except during 1 and 12–13 September when agreement with P_{Q2} is somewhat better. It is interesting to note that P_{RA} lags both P_{AS} and P_{Q2} in five of the six disturbances, the only exception being on 16 September. This phase shift may indicate storage of water in stratiform clouds (Houze, 1977; Leary and Houze, 1979a,b; Frank, 1979). The time-averaged precipitation rate is $\tilde{P}_{AS}$ = 11.9 mm day^{-1} which differs from P_{Q2} by ~15% and is almost identical to P_{RA}. The time-averaged precipitation rates are summarized in Table 1 and the correlations and root-mean-square (rms) differences between the three time series are summarized in Table 2.

Fig. 7 is a time series of the cloud-base mass flux $\mathcal{M}_B(i)$. The ordinate is the cloud-top pressure $\hat{p}$. Maximum values of $\mathcal{M}_B(i)$ for deep clouds are concurrent with maximum values of the forcing for deep clouds shown in Fig. 4. The maxima in deep cloud mass flux on 2, 4–5, 12 and 17 September correspond with days exhibiting qualitatively the strongest observed deep (tops over 10 km) cloud activity (e.g., Houze, 1977; Zipser, 1977; Mower *et al.*, 1979; F. D. Marks, Jr., personal communication, 1980). Shallow clouds, however, tend to occur during undisturbed conditions (e.g., 3, 7–8 and 17–18 September). The time-averaged $\mathcal{M}_B(i)$ (Fig. 8) has a distinct maximum for deep (300 mb) clouds and a secondary maximum for 500 mb clouds. Clouds with tops below 800 mb do not show large amounts of mass flux in the time mean results.

Let the calculated values of the large-scale heat source and moisture sink be defined as

$$(Q_1 - Q_R)_{AS} \equiv c_p\left[\frac{\partial \bar{T}}{\partial t}\right]_{CU}$$

and

$$(Q_2)_{AS} \equiv -L\left[\frac{\partial \bar{q}_v}{\partial t}\right]_{CU},$$

where $[\partial \bar{T}/\partial t]_{CU}$ and $[\partial \bar{q}_v/\partial t]_{CU}$ are the warming

TABLE 1. The time-averaged precipitation rate ($\tilde{P}_{AS}$) for each case and the correlation with estimated precipitation rates from the observed moisture budget (P_{Q2}) and radar (P_{RA}).

		Correlation with	
Case	P_{AS}	P_{Q2}	P_{RA}
Q	11.9	0.887	0.871
N	12.0	0.859	0.862
$F1$	9.1	0.873	0.884
$F2$	0.6	0.729	0.526
$F3$	2.9	−0.379	−0.268
L	13.8	0.861	0.865
$P1$	11.5	0.857	0.855
$P2$	12.3	0.866	0.840
$D1$	12.1	0.886	0.871
$D2$	12.0	0.873	0.877
$R1$	11.9	0.883	0.874
$R2$	9.2	0.893	0.885
$S1$	11.9	0.878	0.873
$S2$	12.6	0.884	0.867

TABLE 2. Correlation coefficients and rms errors between P_{AS}, P_{Q2} and P_{RA}.

Precipitation rate	Correlation coefficient		Root-mean square error	
	P_{RA}	P_{AS}	P_{RA}	P_{AS}
P_{Q2}	0.817	0.887	6.15	5.06
P_{RA}		0.871		5.17

and moistening by cumulus clouds given by

$$\left[\frac{\partial \bar{T}}{\partial t}\right]_{CU} = \sum_{i=1}^{i_{max}} \delta_i[\bar{T}]\mathcal{M}_B(i)$$

and

$$\left[\frac{\partial \bar{q}_v}{\partial t}\right]_{CU} = \sum_{i=1}^{i_{max}} \delta_i[\bar{q}_v]\mathcal{M}_B(i).$$

Fig. 9 shows the time-averaged calculated and observed $Q_1 - Q_R$ (K day^{-1}). The $(Q_1 - Q_R)_{AS}$ and observed $Q_1 - Q_R$ have very similar profiles except just above the SCL top where the calculated values show slight excess warming. The maximum warming is at 600 mb in both profiles. The calculated warming is less than the observed by 0.7–1.6 K day^{-1} above 600 mb but agreement is somewhat closer below. The relative minimum at 500 mb in $(Q_1 - Q_R)_{AS}$ is due to evaporative cooling of detrained suspended liquid water at the cloud-top level.

Fig. 10 shows the time-averaged calculated and observed Q_2 (K day^{-1}). Although $(Q_2)_{AS}$ has a somewhat irregular profile, there is relatively good agreement between the calculated and observed Q_2 values except below 750 mb where $(Q_2)_{AS}$ shows excess drying the equivalent of $\sim$2 K day^{-1}. The irregularities in $(Q_2)_{AS}$ result from the simplifying assumption of detrainment at the cloud-top layer only (Part IV) and the irregularities in the calculated $\mathcal{M}_B(i)$ spectrum (Fig. 8).

b. Case N

In case N, the non-quasi-equilibrium experiment, the mass flux distribution equation takes the following form

$$\left[\frac{dA(i)}{dt}\right]_{OBS} \Delta t = \sum_{j=1}^{i_{max}} [K(i, j)\mathcal{M}_B(j)\Delta t] + F(i)\Delta t,$$

where $[dA(i)/dt]_{OBS}$ is the approximate observed time change of the cloud-work function at time t_0 given by

$$\left[\frac{dA(i)}{dt}\right]_{OBS} = \frac{A_0(i, t_0 + \Delta t_0) - A_0(i, t_0 - \Delta t_0)}{2\Delta t_0},$$

$A_0(i, t_0)$ is the cloud-work function at time t_0 and Δt_0 is the interval between observations. $[dA(i)/dt]_{OBS}$ is defined only when $A_0(i, t_0 + \Delta t_0)$, $A_0(i, t_0)$ and $A_0(i, t_0 - \Delta t_0)$ are positive. Otherwise it is set to zero.

Comparison of cases Q and N directly measures the effect of the cloud-work function quasi-equilibrium assumption on the mass flux distribution function, the cumulus precipitation and the warming and drying due to clouds. Therefore, if the differences between cases Q and N are small compared to the observed estimates, this result may be interpreted as a direct verification of the cloud-work function quasi-equilibrium.

Fig. 11 is a time series of $[dA/dt]_{OBS}$ for each subensemble. Comparison of Figs. 4 and 11 shows that the forcing (F) exceeds $[dA/dt]_{OBS}$ for deep clouds by at least a factor of 5 during almost all disturbed conditions. Similar results were shown in Part I for the Marshall Islands. $[dA/dt]_{OBS}$ is often

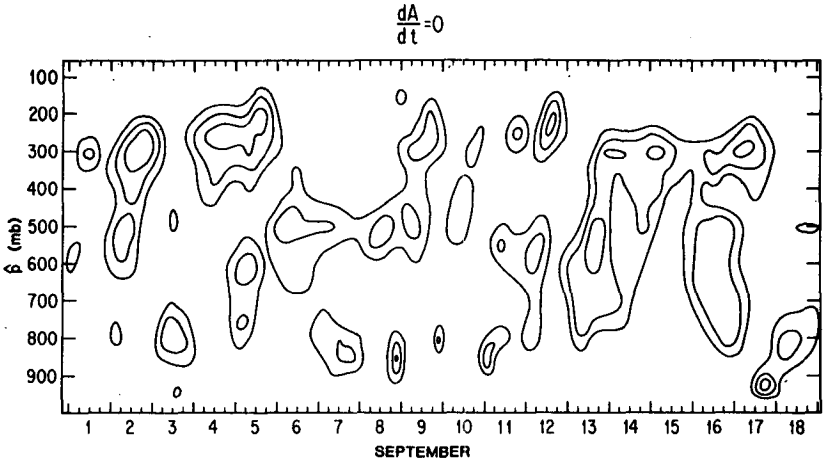

FIG. 7. A time series of cloud-base mass flux (mb h^{-1}) for each cloud type for case Q. The contour intervals are 0.25, 0.5, 1.0, 2.0, 4.0 mb h^{-1}.

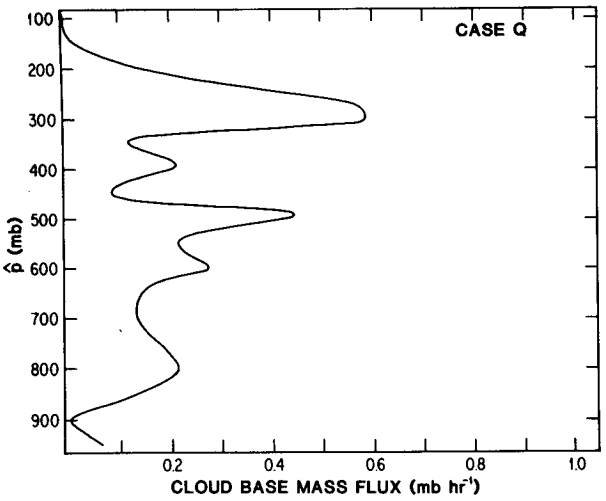

FIG. 8. The time-averaged cloud-base mass flux (mb h^{-1}) for each cloud type for case Q.

the same magnitude as the forcing when the forcing is small. However, under these conditions the cumulus activity is very weak and therefore neglect of $[dA/dt]_{OBS}$ is not likely to result in large errors in the estimation of cumulus effects.

The condition that $|[dA/dt]_{OBS}|/F \ll 1$, however, is necessary but not sufficient for complete verification of the cloud-work function quasi-equilibrium. It is possible that small differences in the vertical distribution of $-F + [dA/dt]_{OBS}$ compared to $-F$ will produce comparatively large differences in the mass flux distribution function depending on the properties of the mass flux kernel. Therefore, to provide a more complete verification of the cloud-work function quasi-equilibrium, the net effect of omitting $[dA/dt]_{OBS}$ on the variables predicted by the parameterization should be examined.

Fig. 12 is a time series of precipitation rates from case N. These calculated precipitation rates also agree with observations well within the observational uncertainties. Comparison of the calculated precipitation rates at each observation time from Figs. 6 and 12 shows that neglect of $[dA/dt]_{OBS}$ produces differences of <10% in almost all instances. The time-averaged precipitation rates of cases Q and N (Table 1) differ by 0.1 mm day^{-1} and the correlations between P_{AS}, P_{Q2} and P_{RA} for case N are slightly lower than for case Q.

Fig. 13 is a time series of the cloud-base mass flux $\mathcal{M}_B(i)$ for case N (cf. case Q, Fig. 7). The principal features of the day-to-day variation in $\mathcal{M}_B(i)$ are the same for cases N and Q. The differences in $\mathcal{M}_B(i)$, most notable for the shallowest clouds, produce only small differences in the time-averaged calculated $Q_1 - Q_R$ and Q_2 when compared with the observed values. Therefore, the cloud-work function quasi-equilibrium assumption is not responsible for the differences between the calculated and observed heat source and moisture sink. The results of case N are strong supporting evidence for the cloud-work function quasi-equilibrium assumption.

c. *Cases F1–F3*

Cases $F1$–$F3$ are designed to show the various components of the cloud-layer forcing. Case $F1$ considers the response of the cumulus ensemble to $(\partial\bar{T}/\partial t)_{ADV}$ while neglecting $(\partial\bar{T}/\partial t)_{RAD}$ and $(\partial\bar{q}_v/\partial t)_{ADV}$ in (5). Case $F2$ considers the response to $(\partial\bar{q}_v/\partial t)_{ADV}$ while neglecting $(\partial\bar{T}/\partial t)_{ADV}$ and $(\partial\bar{T}/$

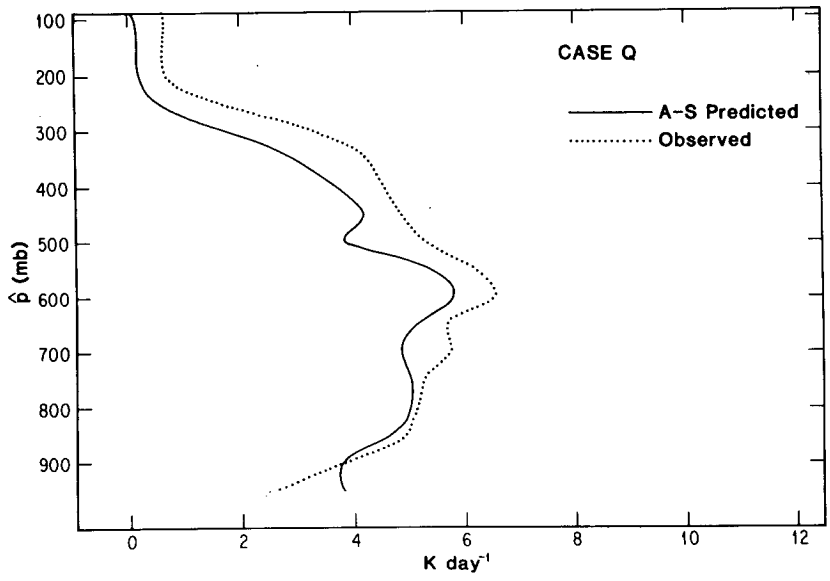

FIG. 9. The time-averaged calculated and observed Q_1–Q_R for case Q.

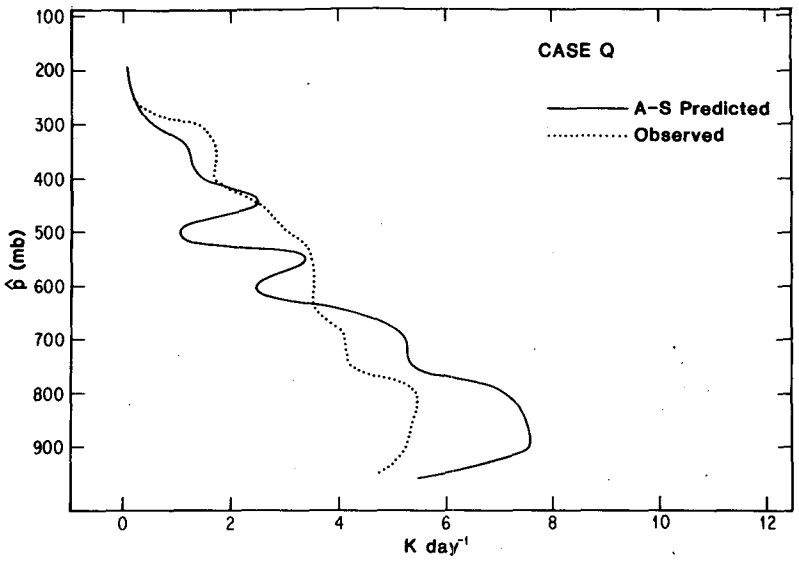

FIG. 10. The time-averaged calculated and observed Q_2 for case Q.

$\partial t)_{\mathrm{RAD}}$. Case $F3$ considers the response to $(\partial \bar{T}/\partial t)_{\mathrm{RAD}}$ while neglecting the advective forcing.

Fig. 14 shows the time-averaged forcing as a function of $\hat{p}$ for each of these cases. For all cloud types the time-averaged advective temperature forcing completely dominates the advective moisture and radiative forcings. Fig. 15 is a time series of precipitation rates for cases $F1$–$F3$. The three curves represent the contributions of the separate forcing functions to the total precipitation rate P_{AS} shown in Fig. 6. The rainfall rates from $F1$ are an order of magnitude larger than the corresponding values for $F2$ during disturbed situations while the precipitation rate due to radiative cooling dominates in suppressed conditions. The time-averaged precipitation rates for these three experiments are given in Table 1. The correlation of P_{AS} with P_{Q2} for $F1$, also shown in Table 1, is somewhat lower than for case Q but is nevertheless highly positive. The correlation for case $F2$ is lower than for $F1$. The radiatively forced precipitation correlates negatively with P_{Q2} and P_{RA}. However, despite this negative correlation, combination of the $F1$, $F2$, and $F3$ (case Q) produces a higher correlation with the P_{Q2} estimate than $F1$ and $F2$ taken separately.

It is important to note that the primary forcing for the *day-to-day* variations in cumulus activity occurs through cooling due to large-scale upward vertical motion. For this time scale the importance of low-level mass convergence in the forcing lies pri-

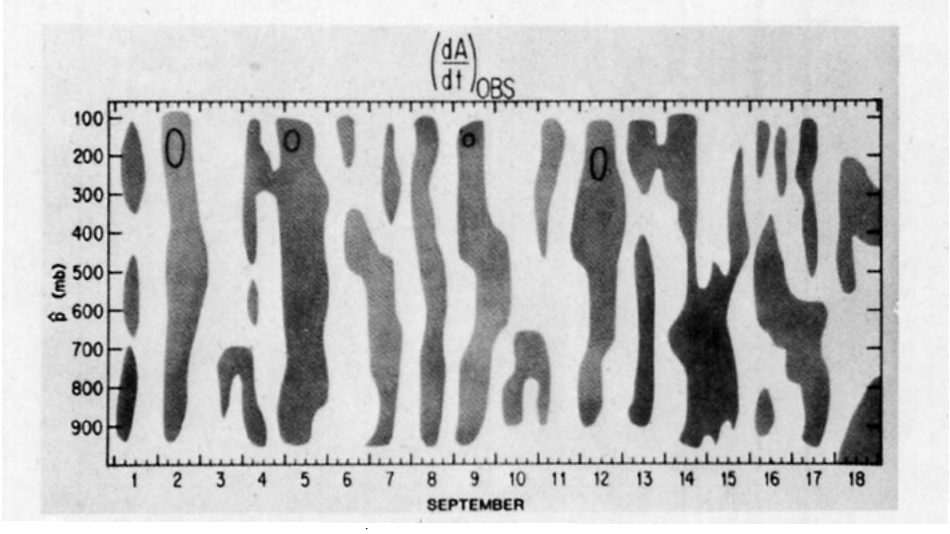

FIG. 11. A time series of $[dA/dt]_{\mathrm{OBS}}$ for each cloud type. The contour interval is 1 kJ kg^{-1} day. The shaded area corresponds to $[dA/dt]_{\mathrm{OBS}} < 0$.

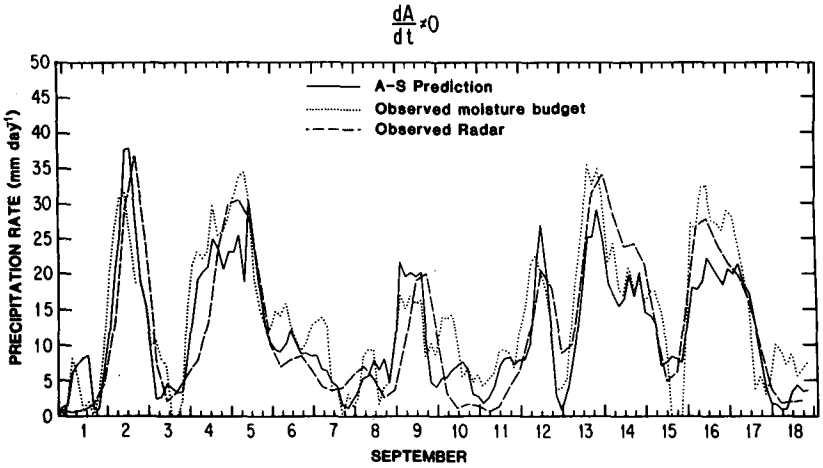

FIG. 12. As in Fig. 6 except for case *N*.

marily in the resultant upward vertical motion and cooling at higher levels in the atmosphere rather than in the moistening due to moisture convergence. Moisture convergence is necessary to maintain a "background" moisture supply; if depletion occurs over the large-scale, q_{vm} and h_m will decrease substantially and the initial cloud-work function $A_0(i)$ may become negative for all subensembles.

d. Case L

Case *L* is designed to illustrate the importance of terms involving the time change of λ in the large-scale forcing. During calculation of $F(i)$ for case *L*, λ is held constant instead of being recalculated from the modified large-scale fields [i.e., $\lambda_0(i)$ is used to calculate $A'(i)$ instead of $\lambda'(i)$, see Fig. 3]. These results for case *L* are essentially the same as those of Lord (1980). Fig. 16 shows the time-averaged large-scale forcing for case *L*. Compared to case *Q*, case *L* shows 30–50% larger forcing for clouds with tops below 300 mb while deeper clouds show approximately the same forcing. As a result, mass flux into shallow- and middle-level clouds predominates and mass flux into clouds with tops above 350 mb is reduced drastically (Fig. 17). Case *L* shows a 16% increase in the time-averaged precipitation rate and slightly lower correlations with observed rainfall estimates (Table 1). More important, however, the calculated cumulus warming and drying (Figs. 18 and 19) show large discrepancies with the observed values. Warming and drying are severely underestimated above 650 mb and severely overestimated below.

It can be shown that λ must increase in order to maintain non-buoyancy at the cloud-top level when cooling due to large-scale upward motion occurs. The resulting decrease in buoyancy production (i.e., forc-

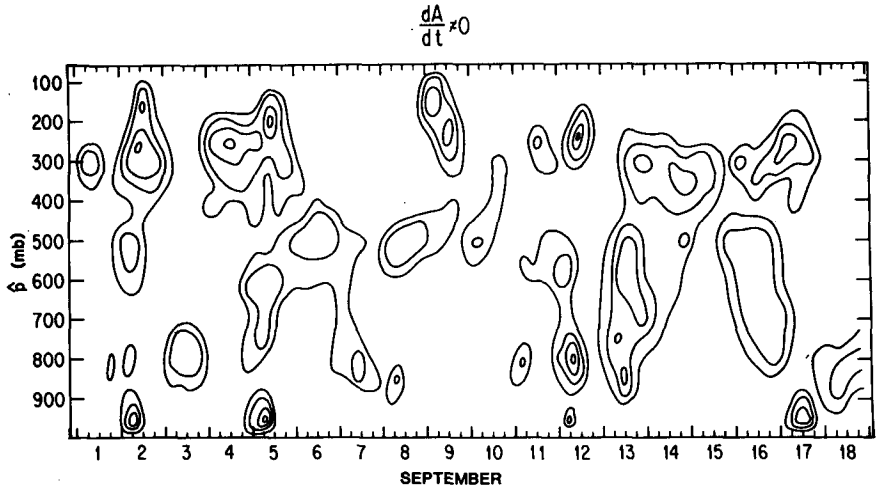

FIG. 13. As in Fig. 7 except for case *N*.

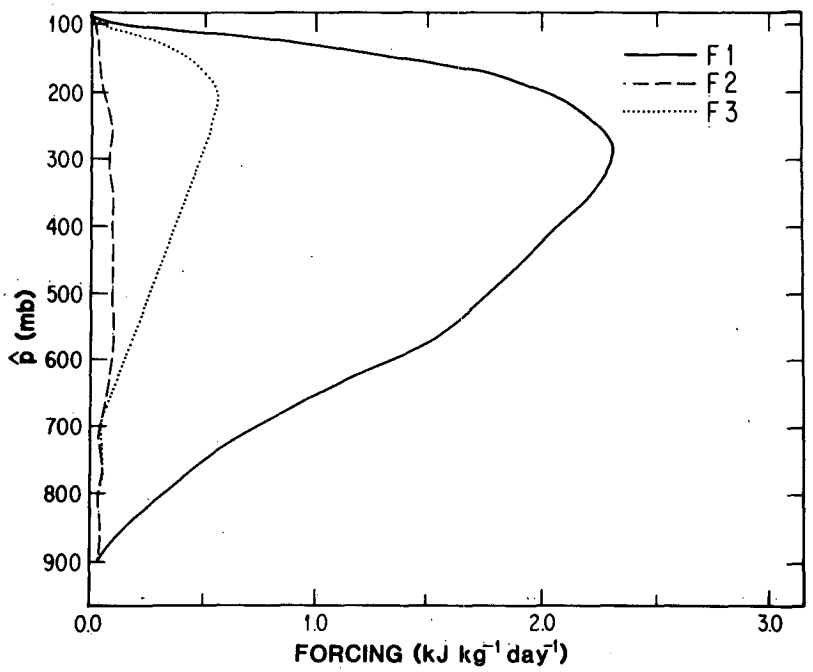

FIG. 14. As in Fig. 5 except for cases $F1$–$F3$.

ing) is greatest for clouds with tops in the 350–650 mb range which have relatively large forcing and relatively large entrainment rates. The results of case L indicate that changes in entrainment, which are necessary to maintain nonbuoyancy at the cloud-top level, play an important role in the prediction of the cloud-base mass flux distribution and the associated vertical distribution of cumulus warming and drying.

e. *Sensitivity experiments*

Several additional experiments were conducted to investigate the sensitivity of this cumulus parameterization to some of the arbitrary parameters and assumptions. The precipitation results are summarized in Table 1.

Cases $P1$ and $P2$ show the sensitivity of the predicted precipitation rates to the choice of the precipitation parameter c_0. Case $P1$ used $c_0 = 0.5 \times 10^{-3}$ m^{-1} and case $P2$ used $c_0 = 3.0 \times 10^{-3}$ m^{-1}. Despite these large percentage changes in c_0 the time-averaged precipitation rates differ from case Q by <5% and the correlations with P_{Q2} and P_{RA} are somewhat lower. The reason is that the normalized precipitation production for each cloud type, given by the product of the first four factors in (11), changes relatively little compared to changes in c_0. Instead the vertical distribution of suspended liquid water for each cloud type is quite sensitive to the value of c_0 (Lord, 1978).

Cases $D1$ and $D2$ show the sensitivity of the pre-

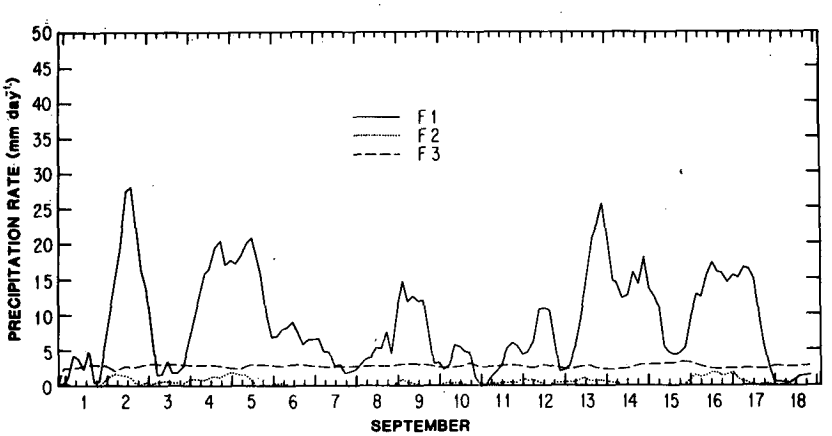

FIG. 15. As in Fig. 6 except for cases $F1$–$F3$.

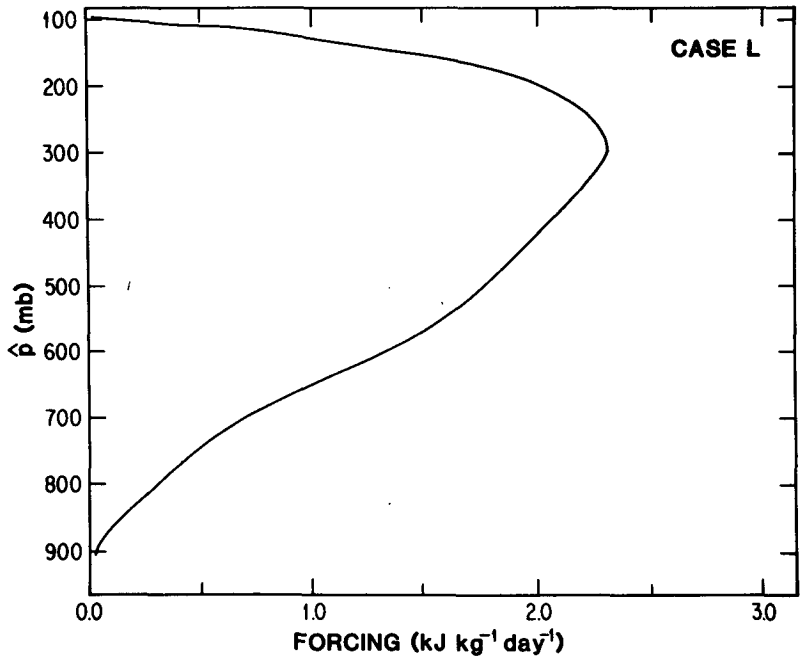

FIG. 16. As in Fig. 5 except for case *L*.

dicted precipitation rates to detrainment of cloud air from the lateral edges of the clouds as formulated by Lord (1978). In that formulation, a fractional detrainment rate λ_d is assumed proportional to the net entrainment rate $\lambda_d = c_d\lambda$, where $c_d = 1.0$ for case *D*1 and $c_d = 3.0$ for case *D*2. A nonzero value of c_d results in very small changes in the time-averaged precipitation rates (Table 1) and the correlations with the observed precipitation rates are very similar to those for case *Q*. The calculated large-scale heat and moisture budgets for cases *D*1 and *D*2 are changed very little from those of case *Q* (Figs. 9 and 10). Therefore, the inclusion of detrainment from the cloud edges is not very important for the prediction

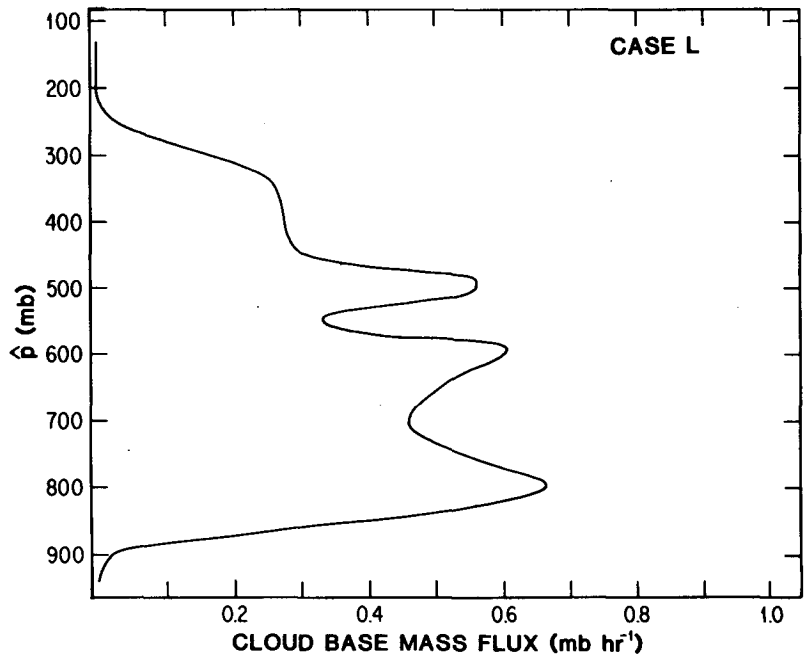

FIG. 17. As in Fig. 8 except for case *L*.

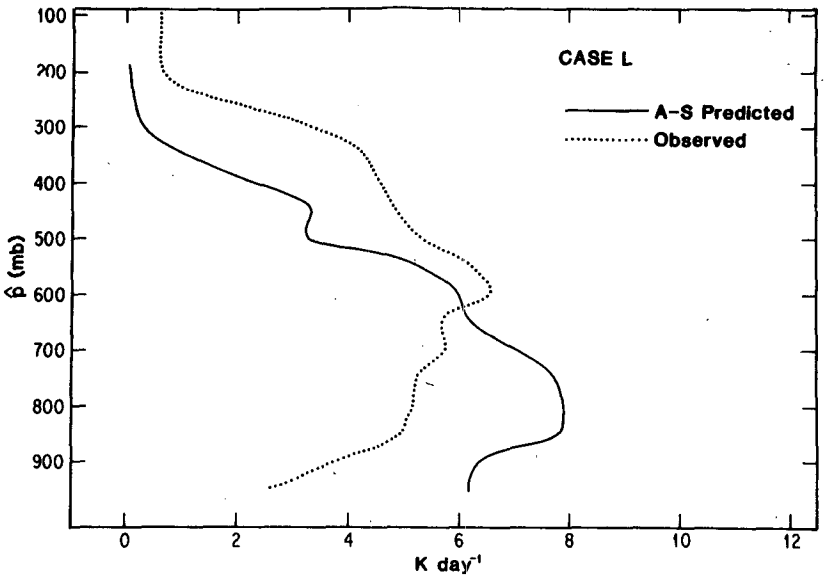

FIG. 18. As in Fig. 9 except for case *L*.

of the vertical profiles of cumulus warming and drying.

The sensitivity of this parameterization to the assumed profiles of radiative cooling is examined in cases *R*1 and *R*2 which uses cooling rates taken from Frank (1977). Case *R*1 uses an estimated cooling rate for a clear atmosphere and case *R*2 uses a vertical distribution characteristic of an atmosphere with deep clouds and cirrus overcast. Fig. 20 shows the time-averaged forcing for each cloud type in cases *R*1–*R*2. The *R*2 profile shows approximately 10–20% smaller forcing than either case *Q* or *R*1 which have almost identical forcing functions. The overall effect of the upper level cirrus is to reduce the radiative cooling rates over the deep layer from the surface to 300 mb. The large cooling at 200 mb exhibited by profile *R*2 seems relatively unimportant for forcing the deep clouds although it may play an important role in enhancing turbulent mixing at the tops of the deep clouds. This effect could be important in determining the persistence of the anvil by governing the local evaporation rate of liquid water. The time-averaged precipitation rate (Table 1) for the cloudy case (*R*2) is ~23% smaller than the rate for case *Q*.

The sensitivity of this parameterization to the so-

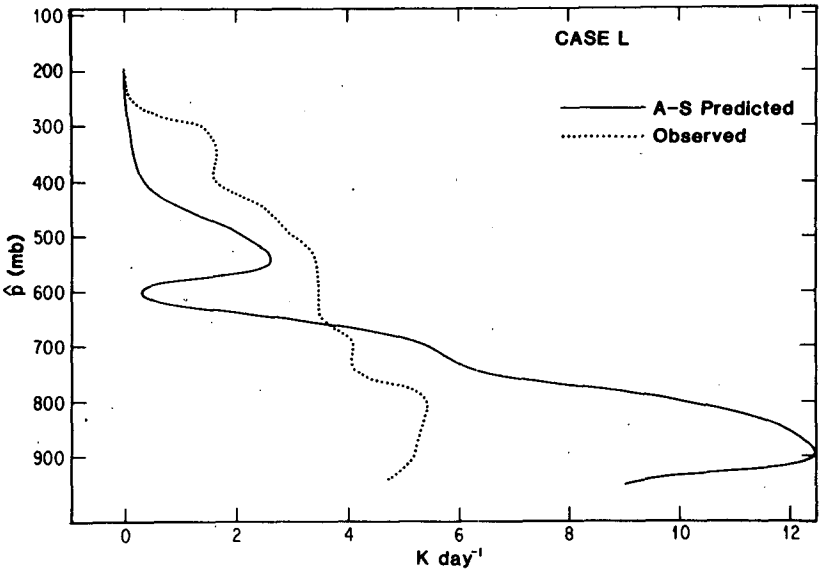

FIG. 19. As in Fig. 10 except for case *L*.

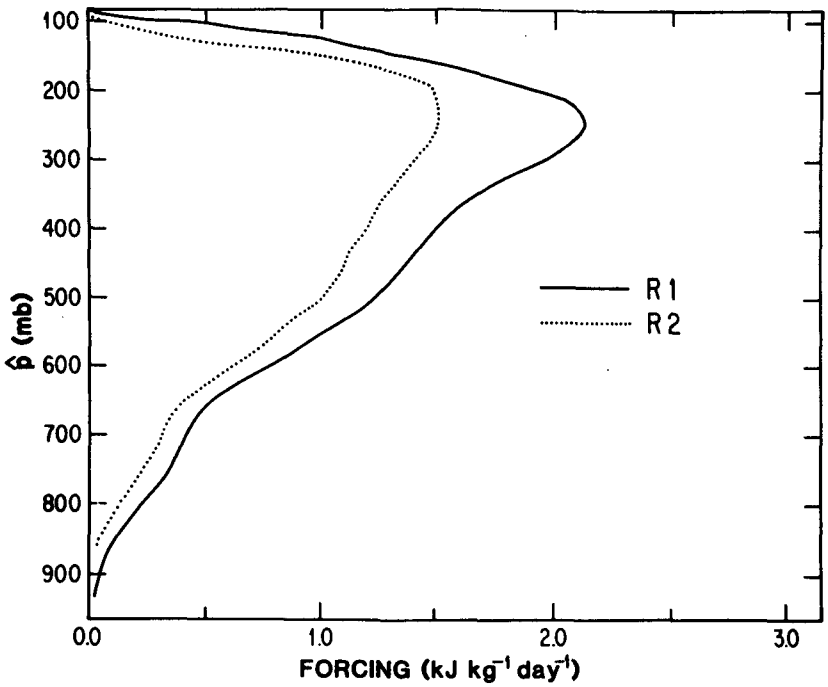

FIG. 20. As in Fig. 5 except for cases $R1$–$R2$.

lution method for the mass flux distribution equation (4) is examined in cases $S1$–$S2$. In case $S1$ the weighting coefficients in the objective function (10) are modified arbitrarily to vary monotonically with cloud type from $c = 0.44$ for the deepest cloud type to $c = 20.0$ for the shallowest. At 93 of the 144 observation times the solutions are identical to those of case Q and consequently the time-averaged precipitation rates are very similar (Table 1). Only seven cases differ by >10% in the calculated precipitation rate; most of the remaining cases differ by <0.2 mm day^{-1} and have quite similar cloud-base mass flux distributions. Thus the solutions of (4) are insensitive to the choice of the c's.

In case $S2$ a direct solution method (see Part IV) is used instead of the simplex method. The time-averaged precipitations are slightly higher than case Q but the correlations are very similar. The shape of the time-averaged cloud-base mass flux distribution is very similar to case Q but shifted to 50 mb deeper clouds. This shift moves the calculated warming and drying closer to the observed above 300 mb and at 500 mb but produces very little change below. These changes do not necessarily improve the results in view of the unknown contributions of mesoscale circulations to the heat and moisture budgets (see discussion in Section 4 below). Furthermore, at almost half of the observation times, the direct solution method produces solutions that do not satisfy (4b) and, therefore, are not physically correct (see the discussion in Part IV). Since the simplex solutions are guaranteed to satisfy (4b), they must necessarily differ from the direct solutions in these cases. It is not possible to determine whether the differences between the solutions are due to errors in the observations or neglect of physical processes (such as cumulus-scale downdrafts) in this parameterization. This experiment indicates that the essential characteristics of the predicted cumulus effects are not overly sensitive to the solution method but that some further investigation is needed.

4. Summary and discussion

The precipitation rates predicted by this parameterization correlate highly with observed estimates and are well within observational uncertainty in both disturbed and undisturbed conditions. These results clearly show that the major interaction between the large-scale thermodynamical processes and the latent heat release by cumulus clouds has been captured by this parameterization. The results of cases $F1$–$F3$ show that the major forcing component of day-to-day variations in cumulus activity is the upper-level cooling (steepening of the temperature lapse rate) due to large-scale upward vertical motion. Comparison of precipitation rates between cases Q and N shows that the cloud-work function quasi-equilibrium is a very good approximation.

The various sensitivity experiments show that this parameterization is rather insensitive to some of its cruder aspects. Cases $P1$–$P2$ and $D1$–$D2$ show that the prediction of cumulus effects is insensitive to the exact value of the precipitation parameter c_0 and the

neglect of detrainment from the sides of clouds. Cases $R1$–$R2$ indicate the maximum sensitivity of this parameterization to the radiative cooling profile. Cases $S1$–$S2$ show some sensitivity to the method of solving the mass flux distribution equation but also emphasize that the essential results of this study do not depend on the solution method.

The time-averaged predicted vertical profiles of warming and drying are quite similar to the observed. Case L indicates that the predicted cumulus mass flux and the associated warming and drying are highly sensitive to changes in the entrainment of air from the large-scale environment which are necessary to satisfy the non-buoyancy condition at cloud top. The discrepancies with observations in case Q, which are of order 1–2 K day^{-1}, may be due to neglect of 1) cumulus-scale downdrafts, 2) the influence of deep mesoscale circulations associated with stratiform rain areas and 3) evaporation and melting in these rain areas. Observational studies of Zipser (1969, 1977), Betts *et al.* (1976), Houze (1977), Zipser and Gautier (1978), and Leary and Houze (1979a,b) from GATE and elsewhere in the tropics have shown that mesoscale circulations are common in areas of deep cumulus convection and that these circulations can contribute significantly to the large-scale heat and moisture budgets. Brown's (1979) numerical modeling study offers a possible mechanism for their generation and maintenance. However, it should be noted that most of these features could be captured by a prognostic model of sufficient resolution which includes both subgrid-scale cumulus parameterization and grid-scale condensation and evaporation processes. The effects of cumulus-scale and mesoscale downdrafts may be especially important in the thermodynamical budgets near cloud base and in the SCL although their exact mechanisms are not well understood and require further investigation. In this study these effects are treated crudely by (8).

Acknowledgments. This paper is based on the author's Ph.D. dissertation submitted to The University of California, Los Angeles and was completed at NHRL, Miami. I extend my sincere appreciation to Professor Akio Arakawa for his advice and encouragement during the course of this research and to Dr. Stanley L. Rosenthal for his support in the completing stages. I thank Professor Richard Reed for providing the data used in this study. I also thank Steven Payne for several stimulating conversations. The helpful comments of R. T. Williams and the anonymous viewers are greatly appreciated, especially the comprehensive and thoughtful criticism of one anonymous reviewer. Thanks are extended to Julia Lueken and Angel Tillman for typing the manuscript, Joe Katz for computing assistance, and Beverly Gladstone and Dale Martin for drafting the figures.

This research was supported by the National Science Foundation and the National Oceanic and Atmospheric Administration under Grant ATM 78-01922, by the Office of Naval Research through the Naval Environmental Prediction Research Facility under Grant N00014-78-C-0103 and by the National Aeronautics and Space Administration through the Goddard Space Flight Center, Institute for Space Studies, under Grant NGR 05-007-328. Computing assistance was obtained from the UCLA Computing and Information Systems, Campus Computing Services, and from the NOAA ERL Computer Services.

REFERENCES

Arakawa, A., and W. H. Schubert, 1974: Interaction of a cumulus cloud ensemble with the large-scale environment. Part I. *J. Atmos. Sci.*, **31,** 674–701.

Betts, A. K., R. W. Grover and M. W. Moncrieff, 1976: Structure and motion of tropical squall-lines over Venezuela. *Quart. J. Roy. Meteor. Soc.*, **102,** 395–404.

Brown, J. M., 1979: Mesoscale unsaturated downdrafts driven by rainfall evaporation: a numerical study. *J. Atmos. Sci.*, **36,** 313–338.

Cox, S. K., and K. T. Griffith, 1978: Tropospheric radiative divergence during Phase III of the GARP Atlantic Tropical Experiment (GATE). Atmos. Sci. Pap. No. 291, Colorado State University, 166 pp.

Deardorff, J. W., 1972: Parameterization of the planetary boundary layer for use in general circulation models. *Mon. Wea. Rev.*, **100,** 93–106.

Emmitt, G. D., 1978: Tropical cumulus interaction with and modification of the subcloud region. *J. Atmos. Sci.*, **35,** 1485–1502.

Frank, W. M., 1977: The structure and energetics of the tropical cyclone II. Dynamics and energetics. *Mon. Wea. Rev.*, **105,** 1136–1150.

——, 1979: Individual time period analysis over the GATE ship array. *Mon. Wea. Rev.*, **107,** 1600–1616.

Gass, S., 1975: *Linear Programming, Methods and Applications.* McGraw-Hill, 406 pp.

Hack, J. J., and W. H. Schubert, 1976: Design of an axisymmetric primitive equation tropical cyclone model. Atmos. Sci. Pap. No. 263, Colorado State University, 70 pp.

Houze, R. A., 1977: Structure and dynamics of a tropical squall-line system. *Mon. Wea. Rev.*, **105,** 1540–1567.

Hudlow, M. D., and V. L. Patterson, 1979: *GATE Radar Rainfall Atlas.* Environmental Data and Information Service, NOAA, Washington, DC, 155 pp.

Johnson, R. H., 1976: The role of convective-scale precipitation downdrafts in cumulus and synoptic-scale interaction. *J. Atmos. Sci.*, **33,** 1890–1910.

——, 1980: Diagnosis of convective and mesoscale motions during Phase III of GATE. *J. Atmos. Sci.*, **37,** 733–753.

Krishnamurti, T. N., Y. Ramanathan, H. L. Pan, R. J. Pasch and J. Molinari, 1980: Cumulus parameterization and rainfall rates I. *Mon. Wea. Rev.*, **108,** 465–472.

Leary, C. A. and R. A. Houze, Jr., 1979a: The structure and evolution of convection in a tropical cloud cluster. *J. Atmos. Sci.*, **36,** 437–457.

——, 1979b: Melting and evaporation of hydrometeors in precipitation from the anvil clouds of deep tropical convection. *J. Atmos. Sci.*, **36,** 669–679.

Lord, S. J., 1978: Development and observational verification of a cumulus cloud parameterization. Ph.D. dissertation, University of California, Los Angeles, 359 pp.

——, 1980: Verifications of cumulus parameterizations using GATE data. *Proceedings of the Seminar on The Impact of*

GATE on Large-Scale Numerical Modeling of the Atmosphere and Ocean. National Academy of Sciences, Washington, DC, 276 pp.

——, and A. Arakawa, 1980: Interaction of a cumulus ensemble with the large-scale environment. Part II. *J. Atmos. Sci.*, **37,** 2677–2692.

——, W. C. Chao and A. Arakawa, 1982: Interaction of a cumulus cloud ensemble with the large-scale environment. Part IV: The discrete model. *J. Atmos. Sci.*, **39,** 104–113.

Mower, R. N., G. L. Austin, A. K. Betts, C. Gautier, R. Grossman, J. Kelly, F. Marks and D. W. Martin, 1979: A case study of GATE convective activity. *Atmos. Ocean.*, **17,** 46–59.

Nitta, T., 1972: Energy budget of wave disturbances over the Marshall Islands during the years of 1956 and 1958. *J. Meteor. Soc. Japan*, **50,** 71–84.

——, 1975: Observational determination of cloud mass flux distributions. *J. Atmos. Sci.*, **32,** 73–91.

——, 1977: Response of cumulus updraft and downdraft to GATE A/B-scale motion systems. *J. Atmos. Sci.*, **34,** 1163–1186.

Ogura, Y., and H. R. Cho, 1973: Diagnostic determination of cumulus cloud populations from observed large-scale variables. *J. Atmos. Sci.*, **30,** 1276–1286.

Ramanathan, Y., 1980: Cumulus parameterization in a case study of a monsoon depression. *Mon. Wea. Rev.*, **108,** 313–321.

Schubert, W. H., 1973: The interaction of a cumulus cloud ensemble with the large-scale environment. Ph.D. dissertation, University of California, Los Angeles, 168 pp.

Thompson, R. M., Jr., S. W. Payne, E. E. Recker and R. J. Reed, 1979: Structure and properties of synoptic-scale wave disturbances in the intertropical convergence zone of the eastern Atlantic. *J. Atmos. Sci.*, **36,** 53–72.

Yanai, M., S. K. Esbensen, and J. H. Chu, 1973: Determination of bulk properties of tropical cloud clusters from large-scale heat and moisture budgets. *J. Atmos. Sci.*, **30,** 611–627.

Zipser, E. J., 1969: The role of organized unsaturated convective downdrafts in the structure and rapid decay of an equatorial disturbance. *J. Appl. Meteor.*, **8,** 799–814.

——, 1977: Mesoscale and convective-scale downdrafts as distinct components of squall-line structure. *Mon. Wea. Rev.*, **105,** 1568–1589.

——, and C. Gautier, 1978: Mesoscale events within a GATE tropical depression. *Mon. Wea. Rev.*, **106,** 789–805.